Journal of Nuclear Materials 400 (2010) 84–93

Contents lists available at ScienceDirect

Journal of Nuclear Materials

journal homepage: www.elsevier.com/locate/jnucmat

The influence of deposited films on the anodic dissolution of uranium dioxide

Derrick Ofori, Peter G. Keech, James J. Noël, David W. Shoesmith *

University of Western Ontario, Department of Chemistry, 1151 Richmond St, London, ON, Canada N6A 5B7

ARTICLE INFO

Article history:
Received 15 October 2009
Accepted 22 February 2010

ABSTRACT

Corrosion product deposits formed over long periods of time could exert a considerable influence on the corrosion rate of used nuclear fuel under permanent disposal conditions. To simulate the build up of such deposits, the oxidative dissolution of UO_2 (nuclear fuel) has been studied under constant current conditions in sodium chloride (pH = 9.5) solutions containing silicate. Currents in the range 1–300 nA cm^{-2} (normalized to the geometric area of the electrode surface) were applied in an attempt to simulate rates as close as experimentally feasible to those anticipated under disposal conditions. The deposits were characterized using scanning electron microscopy, energy dispersive X-ray spectroscopy and Raman spectroscopy. At high currents ($\geqslant$20 nA cm^{-2}) very high potentials ($\sim$0.5 V vs. SCE) were achieved and surface deposits were formed at localized sites on the electrode surface. Raman analyses indicated that these deposits were hydrated uranyl silicates. Their localization was shown to be due to the formation of acidified sites on an otherwise passive surface as a consequence of uranyl ion hydrolysis underneath the deposit. At these sites the local current density was considerably higher than the nominally applied current density. The fraction of the surface covered by a deposit increased as the applied current decreased, leading to a decrease in the extent of acidification. Measurements as a function of applied current density established a potential of $\sim$0.25 V (vs. SCE) as a threshold below which acidification did not occur despite the formation of a deposit. When the current was reduced to 1–2 nA cm^{-2}, the potential ($\sim$0.11 V (vs. SCE)) approached the range of corrosion potentials measured in aerated solutions. These values are well below the threshold potential. Since the maximum corrosion current densities anticipated under actual disposal conditions are <1 nA cm^{-2}, the prospects for acidification leading to enhanced corrosion and radionuclide release rates are very remote.

1. Introduction

The recommended approach for long-term management of used nuclear fuel in Canada is adaptive phased management [1]. This approach includes centralized containment and isolation of the used fuel in a deep geological repository. The Canadian repository concept is based on multiple barriers: the used fuel bundles, durable metal containers, a clay buffer and seals around each container, and a deep stable geologic environment. This deep repository can provide reasonable assurance in the long-term containment and isolation of the fuel. However, it is judicious to consider the consequences of container failure on the fuel corrosion/dissolution and radionuclide release processes.

The groundwater entering a failed container will have a direct influence on fuel corrosion/dissolution and will provide the only medium for radionuclide release from the container and transport through the geosphere to the biosphere [2]. Over the long time scales relevant the containment of nuclear waste (>10^6 y), the rate of fuel corrosion/dissolution will be related to the solubility of uranium in the groundwater; that is, the process will be thermodynamically, rather than kinetically defined. At repository depths, groundwaters are expected to be oxygen-free, and any oxygen introduced during repository construction and operation prior to sealing will be rapidly consumed by mineral and biochemical reactions in the surrounding clays and by minor corrosion of the copper container [3,4]. The subsequent groundwater chemistry will depend on its origin in the host geologic formation. For relevant Canadian Shield crystalline rock, it is expected to be $Ca^{2+}/Na^{+}/Cl^{-}/SO_4^{2-}$ dominated with a pH in the range 6–9. It may also contain small amounts of HCO_3^- 10^{-4}–10^{-3} mol L^{-1} [2].

While groundwater entering the failed container may be anoxic, its radiolysis due to radioactivity in the fuel could produce oxidizing conditions, depending on the time of contact of the groundwater with the fuel, as oxidizing (and reducing) species are continuously produced via radiolysis. Under oxidizing conditions, UO_2 can be oxidized to the +6 oxidation state and dissolve leading to radionuclide release, since the solubility of U^{VI} is many orders of magnitude greater than that of the U^{IV} state [5,6]. The rate of fuel corrosion will depend primarily on redox conditions [7–15] which will be

* Corresponding author. Tel.: +1 519 661 2111 86366; fax: +1 519 661 3022.
E-mail address: pkeech@uwo.ca (D.W. Shoesmith).

0022-3115/$ - see front matter © 2010 Elsevier B.V. All rights reserved.
doi:10.1016/j.jnucmat.2010.02.014

determined by the fuel radiation fields. Since radiation fields decay, redox conditions will evolve and corrosion rates will decay with time. Clearly, the longer the period of containment to prevent wetting of the fuel by groundwater, the lower the rate of production of radiolytic oxidants and the lower the corrosion and radionuclide release rates. If the corrosion/radionuclide release rates are to be determined it is necessary to know the time groundwater contacts the fuel, the redox conditions established by water radiolysis and the influence of groundwater composition.

If fuel corrosion were to persist for a substantial period of time, then corrosion product deposits would accumulate on the corroding fuel surface. This accumulation could have a number of effects:

- It would suppress corrosion by blocking the fuel surface to an extent determined by the porosity of the deposit [16,17].
- It could restrict the diffusive mass transport of species to and from the reacting surface [17]. Since the primary oxidant driving corrosion (H_2O_2) is produced by radiolysis at the fuel surface, a sufficiently thick, low porosity deposit could prevent diffusive loss of H_2O_2 from surface sites. This would maximize its utilization in support of fuel corrosion. Such a deposit could also hinder the access of redox scavengers (Fe^{2+}, H_2 produced by corrosion of the carbon steel container liner [18]) to the corroding surface, thereby reducing the efficiency of H_2O_2 scavenging.
- Deposits could incorporate radionuclides released during fuel corrosion, thereby preventing, or at least delaying, their release to groundwater [19–22].
- By restricting the diffusion of dissolved UO_2^{2+} away from the fuel surface, deposits could lead to a local acidification (via hydrolysis of UO_2^{2+} within pores in the deposit or within defects in the fuel surface (fractures, locations of missing grains, fission-induced porosity) [23,16].

The physical and chemical properties of deposits will be determined by the combination of redox conditions, temperature, and groundwater composition. Key groundwater constituents are CO_3^{2-}/HCO_3^-, which will increase UO_2^{2+} solubility and hinder the formation of deposits, and Ca^{2+} and silicate, which will stabilize insoluble UO_2^{2+} deposits.

The influence of deposits is hard to study on a laboratory timeframe since their rate of accumulation is very slow, especially when redox conditions are only slightly oxidizing. However, similarities in the alteration phases (redeposited dissolved U solids) observed in laboratory experiments and those observed in the geological alteration of natural uraninite deposits [24–28] provides evidence that the overall deposition process observed in the laboratory is similar to the processes likely to control alteration over the repository time frame [29,30].

Most studies on the influence of Ca^{2+} and silicate on the formation of surface deposits have been performed under oxidizing conditions, and demonstrate the incorporation of these species into oxidized uranium phases. Consequently, U^{VI} silicates are expected to be the primary, thermodynamically stable phases formed by fuel alteration under Yucca Mountain (Nevada, USA) conditions [28]. In addition, single-pass flow-through loop experiments and electrochemical studies [31–34] show that the effect of these two species is immediate (after their addition), suggesting a direct effect on the kinetics of the dissolution process as well as on the nature of the deposits formed. Uranium concentrations measured in the flow-through loop experiments with UO_2 pellet fragments showed the corrosion rate to be suppressed by a factor of 200, with the larger influence being exerted by the silicate (up to a factor of 100) [31,32]. A similar suppression of used fuel dissolution rates and radionuclide release rates was also observed [31,32]. A more detailed discussion of deposits has been published elsewhere [34].

In an attempt to form representative deposits on a laboratory time frame, we have employed electrochemical methods to control fuel corrosion rates and surface analytical techniques to determine the composition of the deposits formed. Here, we describe the results of a study performed at low controlled currents in an attempt simulate, as closely as possible, the rates anticipated under repository conditions.

2. Experimental

2.1. Electrode material and preparation

The 1.5 at.% SIMFUEL electrodes used in this study are natural UO_2 pellets fabricated by Atomic Energy of Canada Limited at the Chalk River Laboratories. SIMFUEL is an unirradiated analogue of spent nuclear fuel, made by doping the UO_2 lattice with non-radioactive elements (Ba, Ce, La, Mo, Sr, Y, Zr, Rh, Pd, Ru, Nd) in appropriate proportion to mimic the chemical effects of a CANDU reactor irradiation to 1.5% burnup [35].

A 2–3 mm thick disc was cut from a 12 mm (in diameter) SIMFUEL pellet. A thin layer of Cu was electroplated on one side of the SIMFUEL disc to provide a good electrical contact to the external measuring circuit. The procedure used for Cu deposition has been described elsewhere [36]. The Cu-plated side of the disc was then bonded to a stainless steel threaded post with a conductive silver epoxy (Hysol KS004, Wolcott-Park Inc.). The disc was then encased in a non conductive casting compound (Hysol EE 4183 Wolcott-Park Inc.) so that only one circular face of the electrode is exposed to the working solution. The electrode was then allowed to cure for 24 h at room temperature.

Prior to each experiment, the electrode was polished in succession with 320, 800 (if necessary) and finally 1200 grit SiC paper, and then rinsed with distilled deionized water. The electrode was then placed in a 50:50 distilled, deionized water/methanol solution and ultrasonically cleaned for 2 min to remove any residual SiC and UO_2 debris from the electrode surface. Finally, the electrode was rinsed again with distilled deionized water.

2.2. Solutions

The solution used was 0.1 mol L^{-1} Na_2SiO_3 (Alfa Aesar) + 0.1 mol L^{-1} NaCl (Caledon, 99.0%) (pH 9.5). All solutions were prepared with distilled, deionized water purified using a Millipore Milli-Q-plus unit to remove organic and inorganic impurities, and subsequently passed through Milli-Q-plus ion exchange columns to produce water with a resistivity of 18.2 MΩ cm. Solution pH was monitored with an Orion model 720A pH meter. The pH was adjusted with reagent grade HCl or NaOH.

2.3. Electrochemical cell and equipment

All experiments were performed in a three electrode, single compartment electrochemical cell. The reference electrode was a commercial saturated calomel electrode (SCE) (Fisher Scientific), and all potentials were measured and quoted against the SCE scale (+0.242 V against the standard hydrogen electrode (SHE)). A Pt foil was used as the counter electrode. The cell was housed in a grounded Faraday cage to minimize external sources of noise. Currents were applied using either a Solarton multistat model 1480 (controlled by CorrWare™ software Version 2.9 supplied by Scribner Associates) or a Keithley Precision Current Source Model 6220. To maximize the electrode surface area to solution volume ratio, the electrode (surface area = ~1 cm^2) was submerged in a cell solution volume of only ~50 mL.

2.4. Experimental procedure

Before all experiments the electrode surface was cathodically cleaned for 10 min at −1.60 V (SCE) to remove any air-formed films. A DC current was subsequently applied to the SIMFUEL electrode and the potential response measured as a function of time. At the end of each experiment, the electrode was removed from the cell, lightly rinsed in water and dried, and then analyzed using scanning electron microscopy (SEM), energy dispersive X-ray spectroscopy (EDX), and Raman spectroscopy. SEM/EDX was performed using a Hitachi S4500 field emission SEM. The Raman spectroscopy was carried out using a Renishaw 2000 Raman imaging microscope system. A He–Ne laser beam ($\lambda = 633$ nm) was used as the excitation source operating between 25% and 100% power. The spectra were obtained at an exposure time of 30 s on an extended shift of 120–2000 cm^{-1}, and multiple scans were performed to ensure maximum sensitivity. The laser was focused onto the sample using a 50× uncoated objective lens, at a sample spot size of ~1 μm. Spectra were calibrated using the 520 cm^{-1} line of a silicon wafer and the correct shift was maintained for all scans.

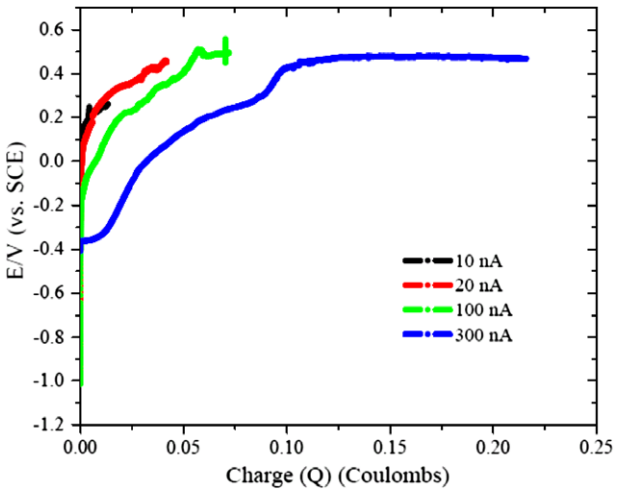

Fig. 2. Charge measured as a function of time for various currents applied to 1.5% SIMFUEL electrodes.

3. Results and discussion

Fig. 1 shows the potential-time profiles recorded for various applied anodic currents ranging from 10 nA to 300 nA. Since the geometric area of the exposed UO_2 surface is ~1 cm^2, these values can be considered as nominal current densities. For the two largest currents, 100 and 300 nA, the potential increased through a series of stages, an effect most apparent in the experiment conducted at 300 nA. At this current, and at short times, the potential exhibits an arrest around ~−0.35 V. A second partial arrest is observed between +0.20 V and +0.30 V, before the potential finally rises to a steady-state value of ~0.50 V. To compare, at 100 nA, these stages are not as well defined, but the first arrest can still be observed around the more positive potential of ~−0.17 V. The arrest between 0.20 and 0.30 V is also still visible and the final rise to the steady-state value is slower than in the experiment conducted at 300 nA. For the 20 nA experiment, the rise in potential towards a final steady-state value of ~0.50 V appears to be occurring but only extremely slowly. Finally, for 10 nA a steady-sate of ~0.25 V appears to be achieved at the termination of the experiment. However, if the experiments are compared on the basis of accumulated charge, obtained by multiplying the applied current by the duration of the experiment ($Q = it$), Fig. 2, it is clear this last experiment did not go long enough to ensure the final steady potential would not eventually rise to 0.50 V, as occurred in the higher current experiments.

Fig. 3 (from Ref. [36]) shows the composition of the electrode surface as a function of applied electrochemical potential determined by X-ray photoelectron spectroscopy (XPS). The stages of oxidation of the UO_2 surface are also noted on the figure. The details of the oxidation process have been discussed elsewhere [36]. The threshold for the onset of oxidation is around −0.40 V (SCE). Initially, the surface is oxidized to UO_{2+x} which involves O^{2-} incorporation and the conversion of U^{IV}–U^{V}. On SIMFUEL this layer is generally very thin (a few nanometers or less). Over the potential range 0 to ~0.30 V the surface is further oxidized to U^{VI}, and, for a sufficiently positive potential, can be considered passive and covered by UO_3 yH_2O. However, if the potential is further increased, passivity is destroyed by the hydrolysis of dissolved U^{VI} (as UO_2^{2+}) leading to the formation of acid and a partial dissolution of this layer [37],

$$UO_2^{2+} + yH_2O \rightarrow UO_2(OH)_y^{(2-y)+} + 2yH^+ \quad (1)$$

$$UO_3 \cdot yH_2O + 2H^+ \rightarrow UO_2^{2+} + (y+1)H_2O \quad (2)$$

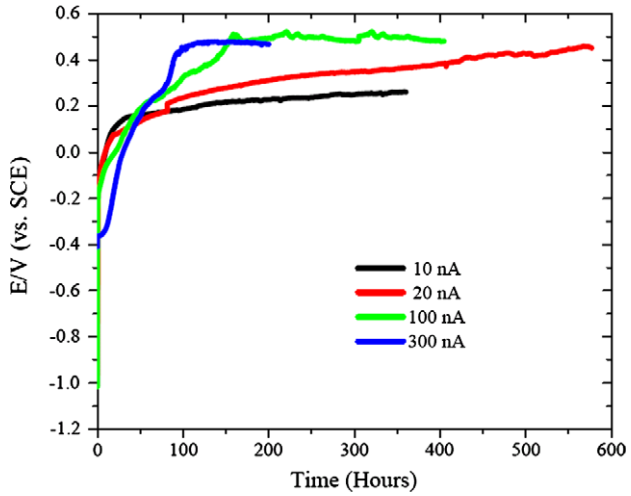

Fig. 1. Potential measured as a function of time for various currents applied to 1.5% SIMFUEL electrodes.

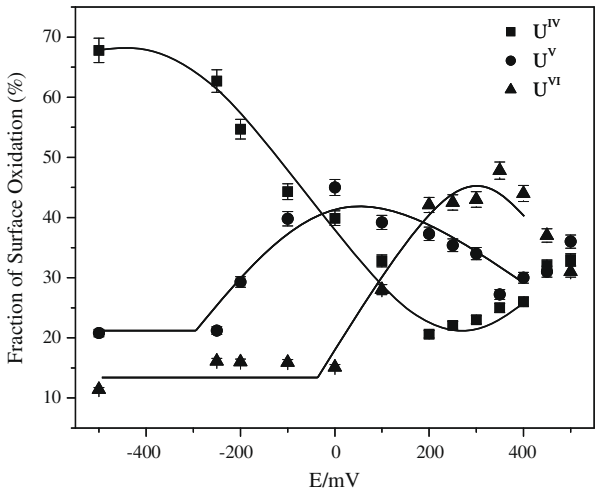

Fig. 3. Relative fractions of U^{IV}, U^{V}, and U^{VI} as a function of applied potential for 1.5 at.% SIMFUEL in 0.1 mol L^{-1} NaCl at pH = 9.5 at room temperature [Santos].

Comparison of the data in Fig. 1 to this compositional plot indicates that the first potential arrest (−0.35 V to −0.100 V) corresponds to the region of surface oxidation to UO_{2+x}, the second arrest (0.20 V–0.30 V) to the region of formation of the "passive" U^{VI} surface layer, and the final steady-state potential of 0.50 V to the onset of acidification. Equally relevantly, electrochemical and XPS studies [33,38] show that, in silicate solutions, a hydrated U^{VI} silicate may be formed over the potential range 0.20 V–0.30 V, and that acidification via reaction 1 is possible once the potential is beyond 0.25 V [37,38]. These observations suggest that for potentials up to 0.25 V a deposit-covered surface would be obtained whereas for higher potentials passivity would be lost and acidification observed. Thus, the achievement of potentials of ~0.50 V for applied currents $\geqslant 20\ nA\ cm^{-2}$ indicates that acidic conditions should have been established on the electrode. However, for an applied current density of $10\ nA\ cm^{-2}$ the potential only reached ~0.25 V and acidification would not be expected in our silicate-containing solutions at the termination of our experiments.

Fig. 4A–K shows SEM images of the surfaces obtained prior to, Fig. 4A, and after experiments at nominal current densities of $20\ nA\ cm^{-2}$ (Fig. 4B–E) and $300\ nA\ cm^{-2}$ (Fig. 4F–K). For both applied currents, a series of different magnifications are shown, and the lighter areas in the images show little evidence for dissolution when compared to an untreated UO_2 surface (Fig. 4A). The darker areas are covered with a deposit, suggesting they have experienced

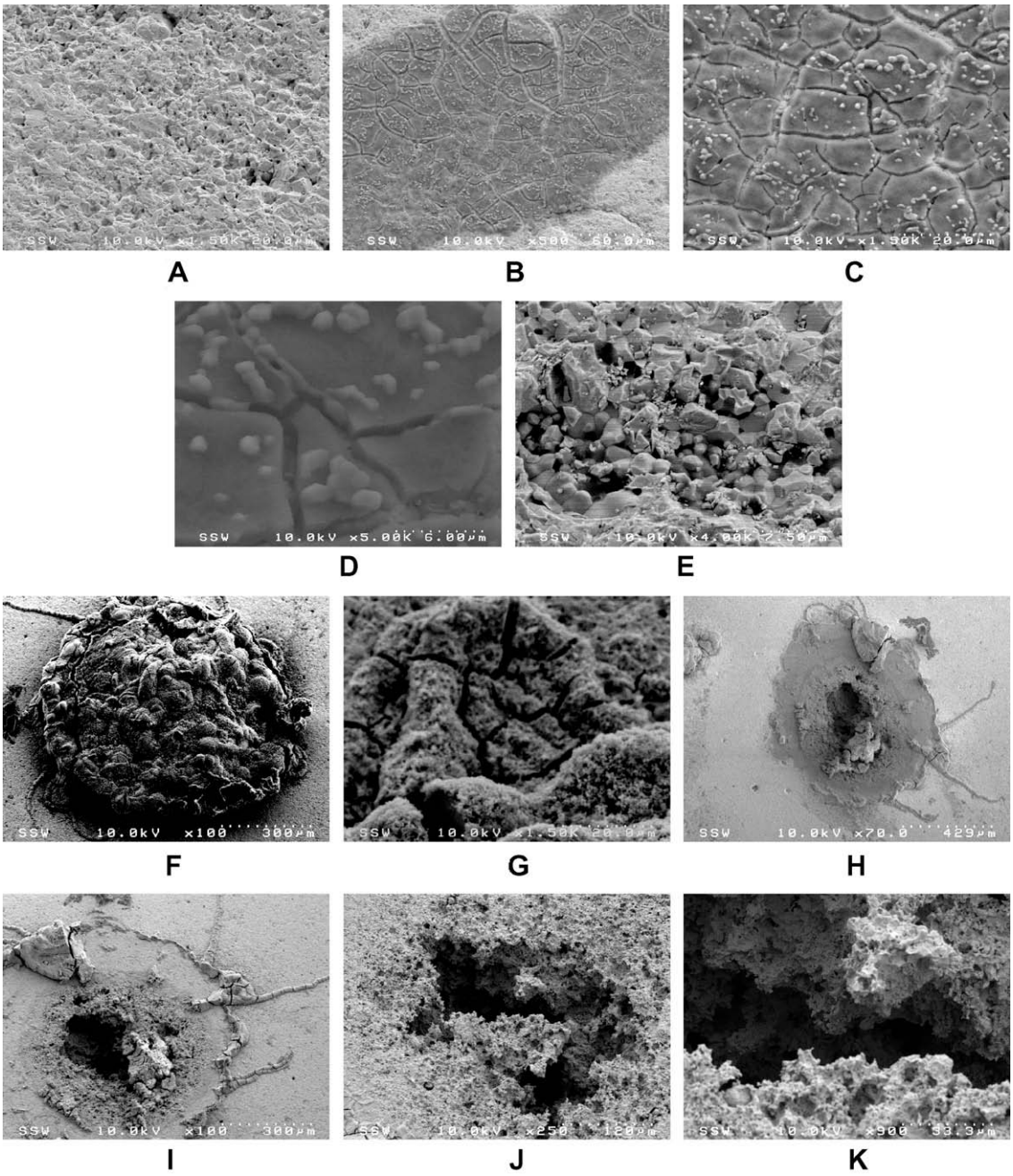

Fig. 4. SEM micrographs of UO_2 specimens before and after oxidation: (A) a freshly polished and sonicated specimen at 1500× magnification; a 20 nA galvanostatic experiment showing uranyl silicate deposits at magnifications of (B) 500; (C) 1500; (D) 5000× magnification; the electrode surface beneath a uranyl silicate deposit after removal of the deposit at (E) 4000× magnification; a specimen after a 300 nA galvanostatic experiment showing uranyl silicate deposits at magnifications of (F) 100; (G) 1500×; the same regions with the uranyl silicate deposits removed at magnifications of (H) 70; (I) 100; (J) 250; and (K) 900×.

dissolution leading to the deposition of a U^{VI} deposit. The fracture patterns observed within this deposit can be attributed to the loss of water due to drying on removal of the electrode from the cell.

Electrochemical experiments conducted voltammetrically or potentiostatically [37,38], indicate that current densities in the range $1–4 \times 10^5$ nA cm^{-2} are obtained for potentials >0.40 V(SCE). Potentials in this range for applied currents as low as 20 nA indicates that current densities capable of sustaining such a positive potential can only be achieved locally. This has been confirmed by low magnification images of the oxidized surface which show only a series of locations covered by deposit accounting for 0.5–1% of the exposed surface. If current densities in the range of $1–4 \times 10^5$ nA cm^{-2} are required to support such a potential then, for an applied current of 20 nA < 0.1% of the surface should be anodically active. This is >50–100 times less than the percentage of the surface which is deposit-covered indicating that not all the area under the deposit is reactive suggesting that reactivity is confined to small areas under, or at the edge, of the accumulating deposit. Examination of the area under the deposit, Fig. 4E, confirms the occurrence of dissolution, as the surface is significantly roughened when compared to Fig. 4A, the untreated sample. Also, the damage is evenly distributed, consistent with an anodic dissolution/deposition process spreading across the surface with reactivity confined to the edges.

By contrast, after anodic oxidation at 300 nA only one active site was observed on the electrode surface, as evidenced by the single large corrosion deposit (Fig. 4F and G) observed following the experiment. Since the total charge passed in this experiment was

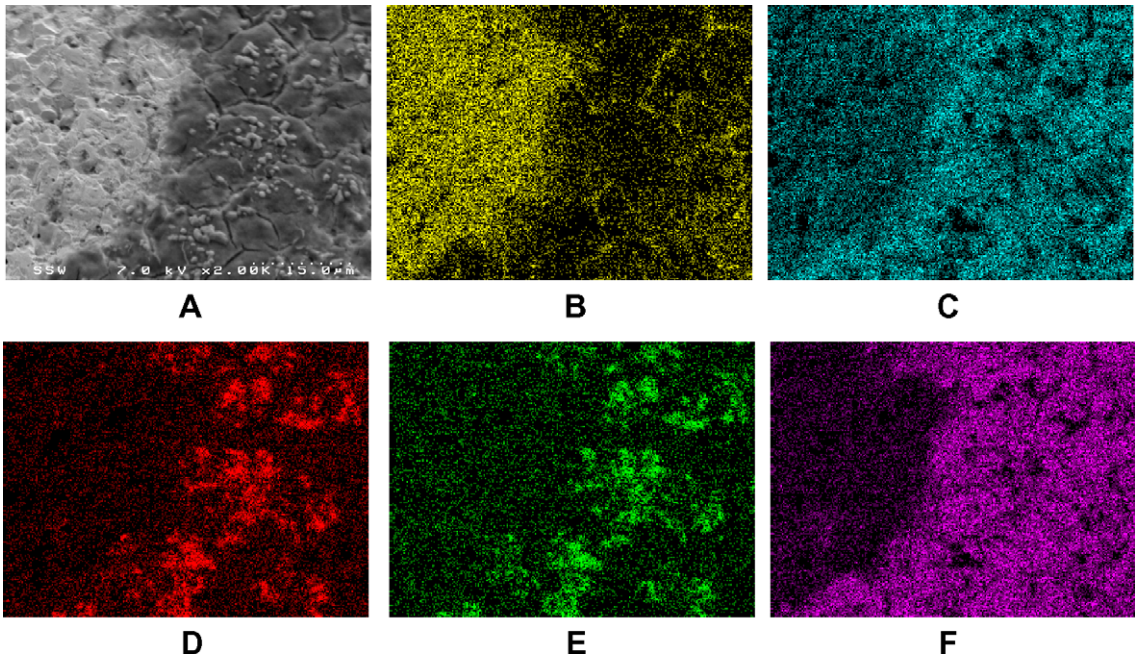

Fig. 5. Specimen after a 20 nA galvanostatic experiment (A) SEM and EDX maps of (B) U, (C) O, (D) Na, (E) Cl, (F) Si content.

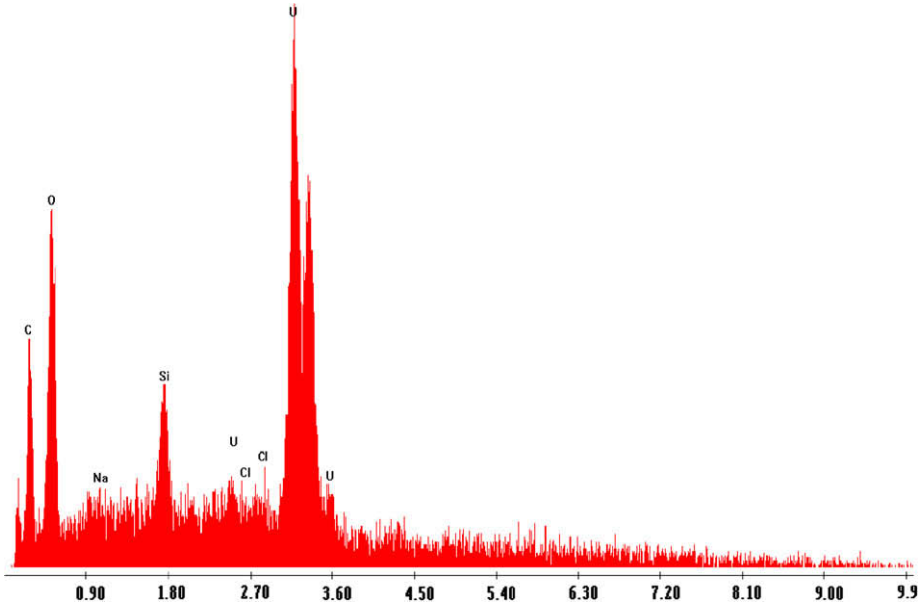

Fig. 6. EDX spectrum recorded on the corrosion product in the 300 nA experiment (Fig. 4F).

three times that passed at 20 nA, considerably more widespread damage would be anticipated. Upon examination of the sample following removal of the corrosion deposit, SEM Fig. 4H–K, shows the damage penetrates inwards rather than across the surface at this higher current density. This is consistent with a localized lower pH and higher anodic dissolution rate leading to deep pitting at this one location.

Fig. 5 shows the results of an SEM/EDX map of an area partially covered by deposit for the 20 nA cm^{-2} experiment. A similar analysis of the deposit present on the surface after the 300 nA cm^{-2} experiment was not possible since the deposit was removed from the single oxidized site on this electrode and analyzed separately. The SEM image (Fig. 5A) shows the surface area over which the elemental maps were obtained. The maps were recorded on a boundary between an apparently unattacked area (the left side) and a deposit–covered area. The signal from the deposit is strong in O and Si (Fig. 5C and F, respectively) and lower in the U (Fig. 5B) than the non-corroded area. This result is consistent with the non-corroded area being UO_2, while the oxidized area is covered by a U^{VI} silicate deposit [38]. The Na and Cl signals (Fig. 5D and E, respectively) associated with the deposit are from the electrolyte and probably left behind when the solution in the deposit evaporated on removal of the electrode from the cell. The inability to remove the NaCl from the deposit region via washing the electrode suggests the presence of electrolyte within pores in the deposit, as NaCl was not observed on the non-corroded UO_2 regions.

Fig. 6 shows a spot EDX analysis of the deposit formed in the experiment at 300 nA cm^{-2} (Fig. 4F) and Table 1 lists the atomic percentages in the deposit. These data indicate a deposit with U:Si:O ratio of 1:1:5, consistent with the presence of uranyl silicate. Also, the imbalance between Na and Cl contents in the deposit suggests the incorporation of Na^+ into the silicate. Unfortunately, a definitive identification of the nature of this deposit based only on these analyses is not possible. To date, 14 uranyl silicate minerals have been characterized [39], of which nine have a U:Si ratio of 1:1. The exact structures of these silicates are not completely understood, due to uncertainty in the nature of the water present (H_2O, H_3O^+, OH^-), but the uranyl ion is generally co-ordinated with five oxygen atoms in the equatorial plane to form a pentagonal bipyramid [40–42].

Fig. 7 shows Raman spectra recorded on the fresh UO_2 surface (A) and on the deposit (B) formed at 300 nA cm^{-2}. Raman spectra recorded on single crystal UO_2 [43,44] show that stoichiometric UO_2 has a single fundamental vibrational stretch around 448 cm^{-1}. In addition, a broad peak near 1150 cm^{-1} has been reported [40,47,49,50], and attributed to a crystal field transition ($\Gamma_5 \rightarrow \Gamma_3$). Raman spectra recorded on polycrystalline UO_2 [45] showed an unassigned peak at 585 cm^{-1} attributed to a damaged UO_2 matrix due to bulk defects resulting in a breakdown of selection rules. All of these features are present in the spectrum recorded on the fresh UO_2 surface, Fig. 7A.

Table 1
Composition of the deposit formed on SIMFUEL at a current of 300 nA determined by EDX analysis.

	O	Na	Cl	U	Si
At.%	65.58	3.68	0.97	15.11	14.66

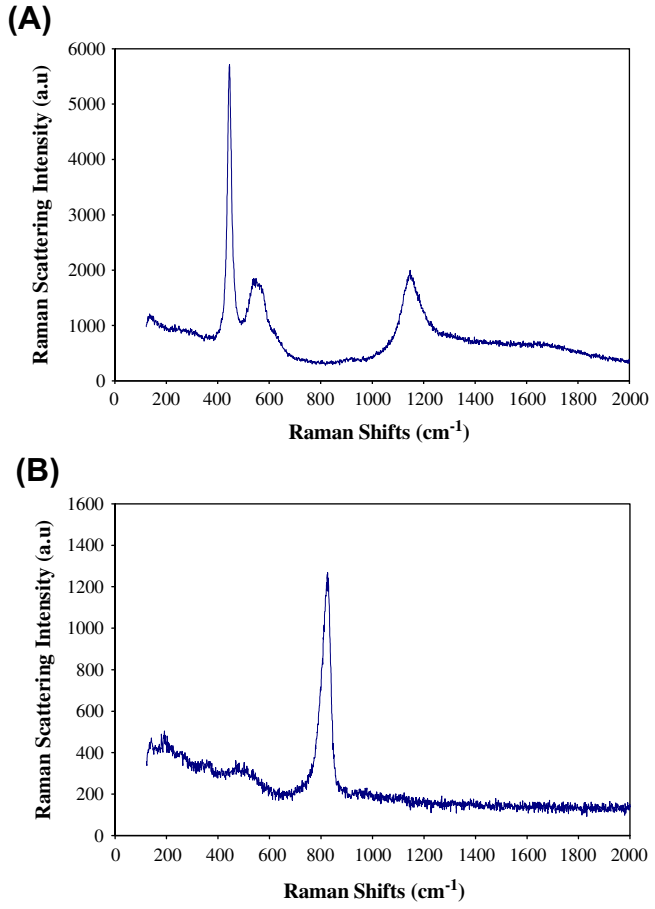

Fig. 7. Raman spectrum of (A) bulk UO_2, (B) the thick corrosion product deposit formed in the 300 nA Long Term Galvanostatic experiment.

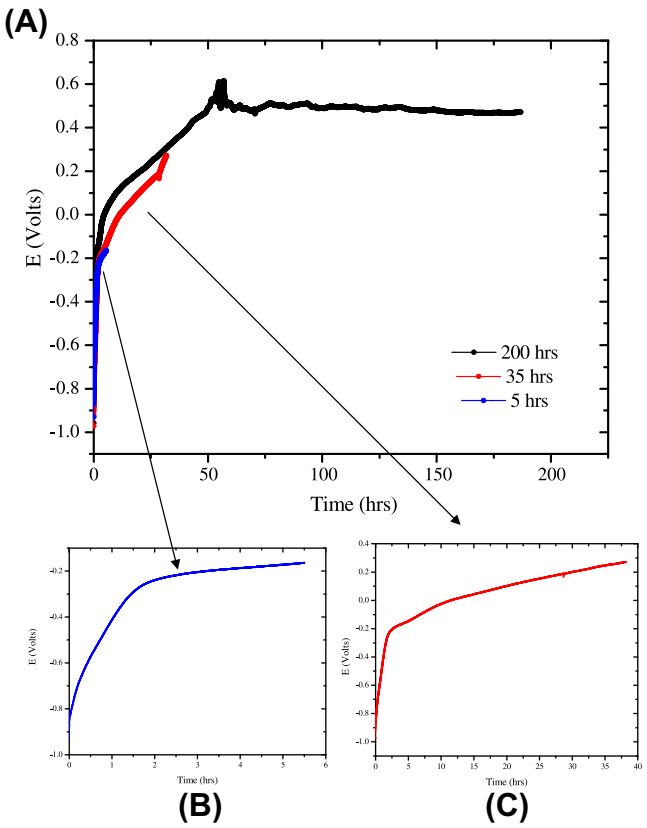

Fig. 8. (A) Potential-time profiles recorded in long-term experiments at an applied current of 300 nA for various durations. Expansions of the time scale for the 5–6 h experiment and the 35–40 h experiment are shown in (B) and (C), respectively.

Raman spectra of uranyl compounds, such as dehydrated schoepite (UO_3 $0.8H_2O$), exhibit a peak centered around 842 cm^{-1} attributed to the symmetric stretching mode of the uranyl ion, $(O–U–O)^{2+}$ [46,40]. However, the frequency of this stretch is sensitive to factors such as the type of equatorial bonding ligands present [46] and, in general, occurs between 800 and 850 cm^{-1} [46,47]. Thus, the peak centered at 829 cm^{-1}, Fig. 7 B, may be attributable to the presence of uranyl species in the deposit. The ill-defined signals in the low wavenumber region can be attributed to the bending vibrations of UO_2^{2+} (200–340 cm^{-1}) [48–51].

Generally, the Si–O–Si bending mode and the Si–O asymmetric stretching vibrational mode of SiO_4^{4-} tetrahedra are observed in the wavenumber ranges 600–800 cm^{-1} and 800–1200 cm^{-1}, respectively [52]. The high frequency band can be further separated into four subpeaks associated with the Si–O stretching frequency in different polymerized species [52]. However, no peaks that could be attributed to silicate were observed in the spectra recorded on the corrosion product deposit, Fig. 7B. Also, the silicate present in the solution showed no Raman activity for reasons which are not understood.

The ideal SiO_4^{4-} tetrahedron would have T_d point group symmetry, a Raman inactive structure. However, this could potentially be lost by protonation to $(SiO_3OH)^{3-}$ when the pH of the initially basic silicate solution is adjusted to 9.5. This protonation, together with bonding of the remaining three oxygens in the uranyl silicate, could lead to a lowering of $(SiO_3OH)^{3-}$ symmetry ($T_d \rightarrow C_{3r} \rightarrow C_S$) [53]. This could deactivate some allowed transitions, also making

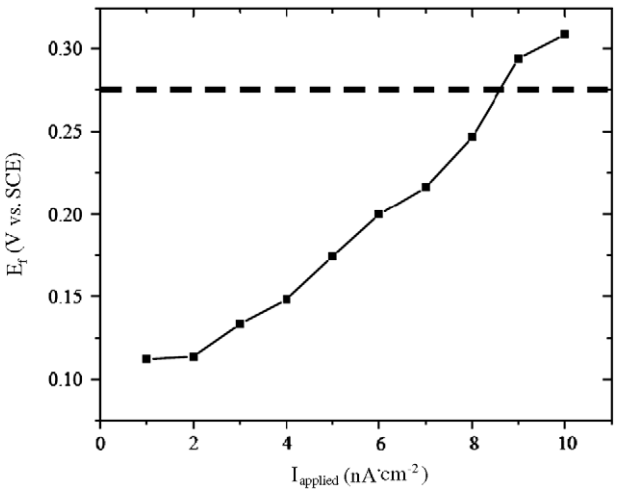

Fig. 10. Final potentials recorded on 1.5 at.% SIMFUEL in the Chronological Current Increment experiment beginning at 1 nA as a function of the applied current. The horizontal dashed line shows the threshold for the onset of acidification.

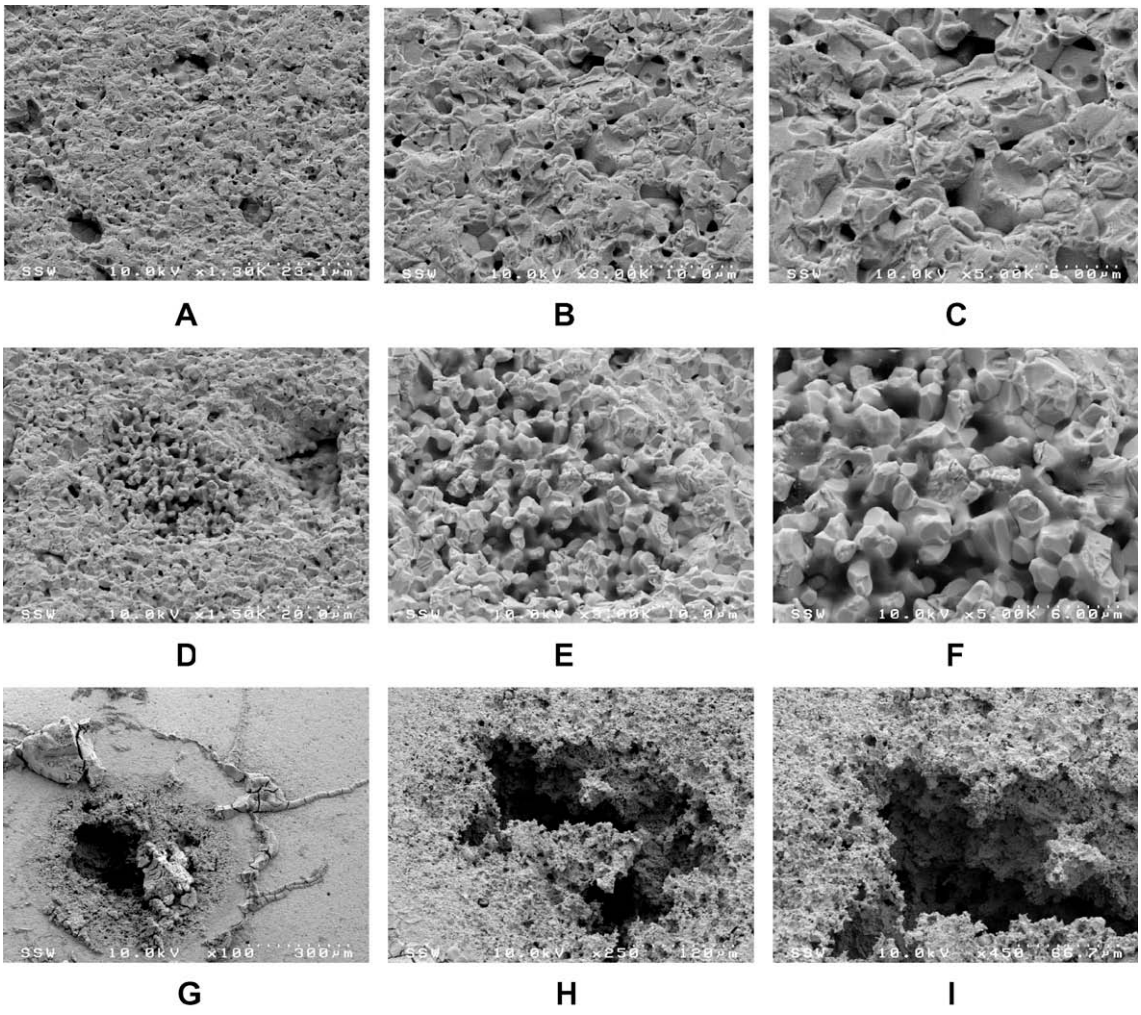

Fig. 9. SEM images of the electrode surface after 300 nA galvanostatic experiments for: 5.5 h at: (A) 1300, (B) 3000 and (C) 5000× magnification; 37 h at (D) 1500, (E) 3000 and (F) 5000×; and 190 h at (G) 100, (H) 250 and (I) 450× magnification.

them Raman inactive. A second possibility is an overlapping of the stretching vibrational modes for UO_2^{2+} (800–900 cm^{-1}) and SiO_4^{4-} (819 cm^{-1}) as observed for soddyite ((UO_2) $2SiO_4$. $2H_2O$) [53].

To investigate the significance of the potential stages observed (Fig. 1), a series of experiments of different durations was performed with an applied current of 300 nA, Fig. 8A. The individual stages are not as clear in this plot, but the expanded plots for the two shorter experiments show that, after 5.5 h the potential achieved a plateau value of −0.20 V (SCE), Fig. 8B, and after 37 h, ~0.25 V (SCE), Fig. 8C. As occurred in the experiment shown in Fig. 1, a steady-state potential of ~0.50 V (SCE) was achieved when the experiment was extended beyond 50 h.

Fig. 9 shows SEM micrographs of the electrode surface after each of these experiments at a series of magnifications: A–C, D–F, and G–I for 5.5, 35 and 200 h experiments, respectively. After 5.5 h, Fig. 9A–C, there is no noticeable difference between the electrochemically oxidized and the freshly polished surfaces, Fig. 4A, indicating little dissolution had occurred. The correlation between surface oxidation state and potential, as measured using XPS (Fig. 3) would suggest such a result, as −0.20 V was found to produce a sample that was predominantly covered by U^{IV}. After 37 h there is again no SEM evidence for the formation of a deposit under which localized acidification could have occurred; although, as shown in Fig. 9D and E, some areas of the surface have under gone significant dissolution. However, after ~190 h, deep local penetration of the surface has occurred, as previously observed at this applied potential [37], indicating the occurrence of localized dissolution at an acidified location. These observations are consistent with the claim that potentials ⩾0.25 V are required before the development of localized acidification leading to major deposition occurs.

To define a current threshold and further probe the potential threshold for the onset of acidification, the potential–time behavior was followed in an experiment through which the applied current was systematically increased from 1 nA to 10 nA in 1 nA increments, the final potentials for which are plotted in Fig. 10. The maximum potential achieved after application of the final, and highest, current of 10 nA was ~0.30 V: near the threshold where acidification has been described to occur [37]. Fig. 11 shows low (A–C) and high (D–H) magnification SEM micrographs of the electrode surface upon completion of the experiment. Crudely, light (uncovered) and dark (covered) areas are observed, with darker areas dominating the surface coverage (i.e. deposit coverage >80%). Close inspection (Fig. 11D–H) shows that where dark areas of the surface exist, there is a thin, compact deposit, while the lighter areas are uncovered and lightly etched, Fig. 11E. The compact deposit appears extremely fine–grained and very widespread; hence, it would be expected to be protective to a naturally corroding system. The observable network of fractures in Fig. 11 is typical mudcracking patterns, and can likely be attributed to loss of water on removal from the cell and drying.

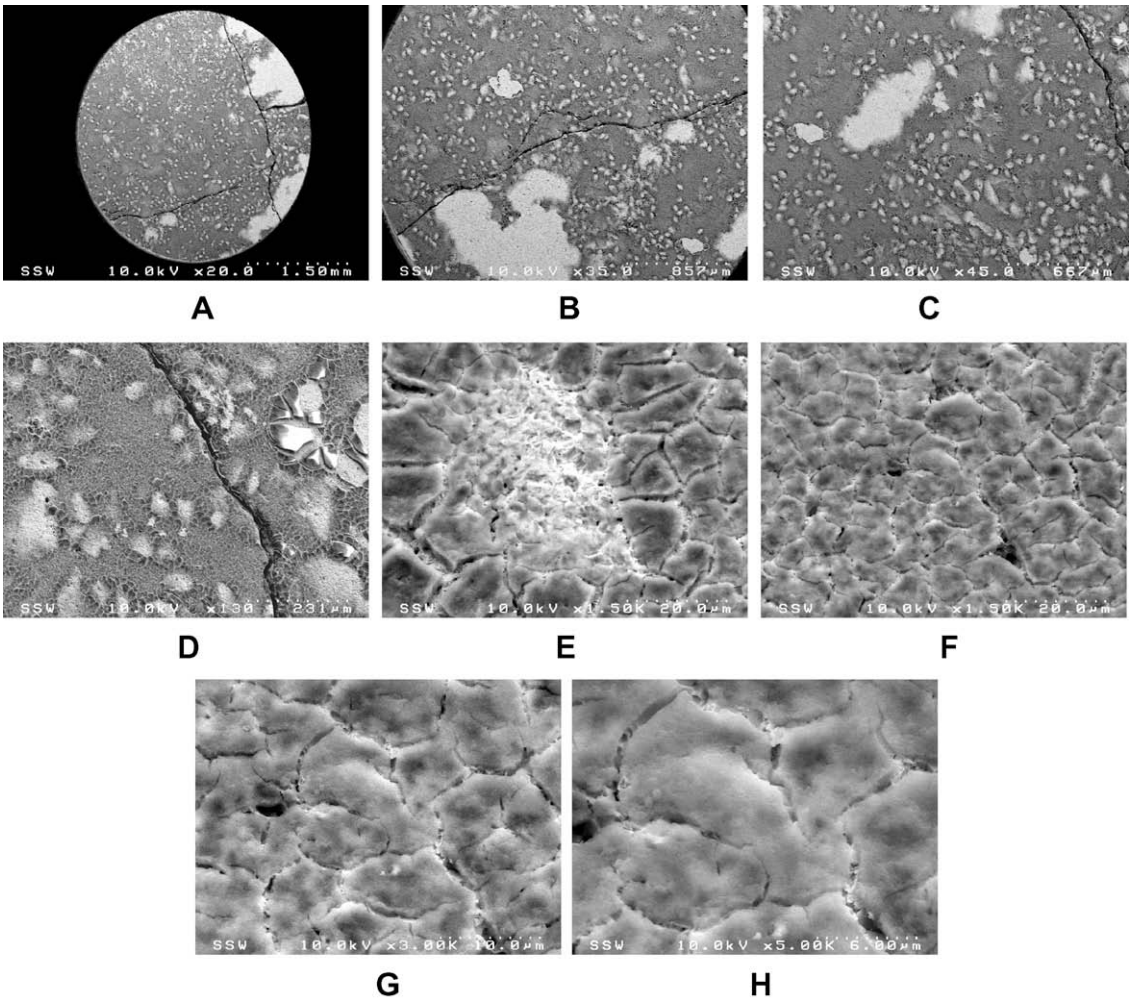

Fig. 11. SEM images of the electrode surface recorded after the Chronological Current Increment experiment beginning at 1 nA for magnifications of (A) 20, (B) 35 and (C) 45, (D) 130, (E) 1500, (F) 1500, (G) 3000 and (H) 5000×.

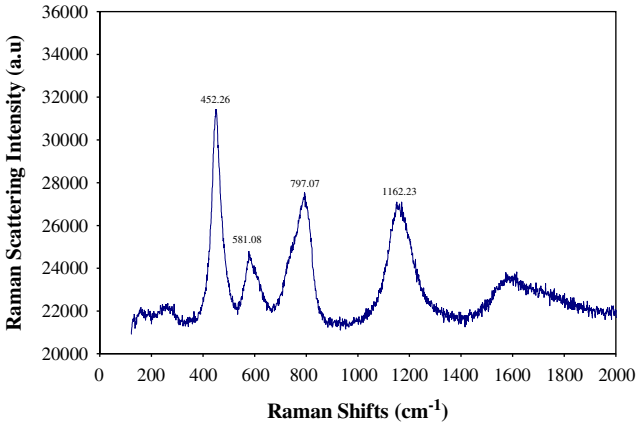

Fig. 12. Raman spectra of the SIMFUEL electrode surface after the Chronological Current Increment experiment beginning at 1 nA.

Fig. 12 shows a Raman spectrum recorded on an area of the surface covered by the fine deposit. The pattern appears to be a combination of those observed in Fig. 7A and B: the UO_2 peaks at 450, 1150 and 580 cm^{-1} (the fundamental vibrational stretch, the crystal field transition and the damaged matrix, respectively); and, the UO_2^{2+} or $SiO_3(OH)^{3-}$ stretch at ~800 cm^{-1}, also described above. Where no deposit exists on the surface, Raman spectra were consistent with Fig. 7A, the unreacted UO_2 surface. The ongoing appearance of these light-coloured (in the SEM images), etched areas on the electrode surface verifies the existence of areas at which anodic dissolution continues as the applied current is increased. As the current increases the dissolution process would be expected to become increasingly more localized at these regions as the remaining electrode becomes increasingly covered. The absence of thick deposits at these locations at the point of analysis indicates that the ongoing slow loss of soluble U^{VI} is favourable and confinement/acidification is minimal. Removal of the deposit via sonification-rinsing confirms these observations, as the entire UO_2 surface can be seen to be generally attacked/etched. Some areas show enhanced dissolution has occurred, as attack/etching is non-uniform; this would suggest that some areas of the surface may have experienced slight acidification underneath the deposit.

As indicated, Fig. 10 plots the final potential achieved as a function of applied current. The horizontal dashed line shows the tentatively established acidification threshold at 0.28 V, established through our experiments. Thus, it is likely that any tendency towards local acidification leading to the enhanced dissolution occurred at the higher current densities (9, 10 nA) when the potential exceeded this threshold. Of course, as Fig. 1 would indicate, a significant time delay may precede such acidification, as 400 h was insufficient for 10 nA to exceed 0.25 V in the experiment described therein. However, of equal interest, is the potential at the lowest applied currents. For a current $\leqslant$2 nA, the potential approaches a plateau at a value of ~0.11 V (SCE), which is in the range measured for the corrosion potential of UO_2 and SIMFUEL in aerated [54–58], peroxide-containing (10^{-4}–10^{-2} mol L^{-1}), and alpha-radiolytically decomposed solutions [56] at this pH. This last natural corrosion process has been studied in detail [54–58], and electrochemical and surface analytical evidence indicates that the rate determining reaction is the slow release of U^{VI} (UO_2^{2+}) from a UO_3 yH_2O-covered surface. Based on extrapolation of electrochemically measured anodic dissolution rates [7], the predicted corrosion rate in this potential region is in the range 0.1–1 nA cm^{-2}, which is slightly lower than the applied currents of 1–10 nA cm^{-2}. A more detailed model for alpha radiolytic corrosion of fuel inside a failed waste container [10] predicts an evolution of corrosion potential decreasing from −0.50 V (SCE) to −0.18 V (SCE) over a 30,000 year period, and lower currents. All of these values are substantially lower than those measured in the experiments discussed in this paper, where acidification did not occur at our lowest applied currents. Consequently, we can conclude that, irrespective of whether noble metal particles can act as preferential cathodes leading to the separation of anodes and cathodes, the development of acidified anodic locations in the fuel through natural corrosion processes is extremely unlikely.

4. Summary and conclusions

1. Under controlled current conditions the oxidation of UO_2 proceeds through three potential stages: (i) between −0.4 V and −0.1 V, a non-stoichiometric layer of UO_{2+x} is formed; (ii) dissolution as UO_2^{2+} and the formation of a surface layer of UO_3 yH_2O over the potential range 0 V to ~0.25 V; and (iii) hydrolysis of dissolved UO_2^{2+} and the formation of locally acidified sites for potentials more positive than +0.25 V.
2. In the silicate solution used in these experiments, dissolution as UO_2^{2+} leads to the formation of a uranyl silicate deposit which confines local acidity underneath the deposit.
3. The extent of surface coverage by such a deposit and the amount of dissolution supported beneath it varies with the applied current. At high currents only a small number of localized sites become acidified and deep penetrations occur beneath the uranyl silicate deposit. At lower applied currents, the deposit is more widely spread across the UO_2 surface and active dissolution is confined to the edges of the deposit-covered areas.
4. Based on a series of experiments in which the applied current was increased in stages from 1 to 10 nA cm^{-2}, a current of >8nA cm^{-2} was required for the potential to exceed the threshold for acidification of ~+0.25 V.
5. For applied currents in the region of 1–2 nA cm^{-2} the potential achieved is ~0.11 V, which is in the range of measured corrosion potentials in aerated solutions. Since the maximum predicted corrosion rate under waste disposal conditions is 0.1–1 nA cm^{-2}, the prospects for the formation of locally acidified sites under waste disposal conditions is very remote [17].

References

[1] Nuclear Waste Management Organization (NWMO), Choosing a Way Forward: The Future Management of Canada's used Nuclear Fuel. www.nwmo.ca.
[2] J. McMurry, Reference Water Compositions for a Deep Geologic Repository in the Canadian Shield, Ontario Power Generation Report No. 06819-REP-01200-10135-R01, 2004.
[3] J. McMurry, D.A. Dixon, J.D. Garroni, B.M.Ikeda, S. Stroes-Gascoyne, P. Baumgartner, T.W. Melnyk, Evolution of a Canadian Deep Geologic Repository, Ontario Power Generation Report No. 06819-REP-01200-100092-R00, 2003.
[4] M. Kolar, F. King, Modelling the consumption of oxygen by container corrosion and reaction with Fe(II), In: W.M. Murphy, D. Knecht (Eds.), Proc. of the XIXth International Symposium on Scientific Basis for Nuclear Waste Management, Boston, November 27–December 1, 1995, Mat. Res. Soc. Proc., vol. 412, Pittsburgh, PA, 1996, pp. 555–567.
[5] J. Grenthe, R.J. Fuger, R.J. Konings, A.B. Lemire, C. Muller, H. Nguyen-Trung, Wanner, Chemical Thermodynamics of Uranium, North Holland, Amsterdam, 1992.
[6] R. Guillamont, T. Fanghanel, I. Grenthe, V. Neck, D. Palmer, M.H. Rand, Chemical Thermodynamics, vol. 5, Elsevier, Amsterdam, 2003.
[7] D.W. Shoesmith, J. Nucl. Mater. 282 (2000) 1–31.
[8] L.H. Johnson, D.M. LeNeveu, F. King, D.W. Shoesmith, M. Kolar, D.W. Oscarson, S. Sunder, C. Onofrei, J.L. Vrosthwaite, Atomic Energy of Canada Report, AECL-11494-2, COG-95-552-2, 1995.
[9] L.O. Werme, L.H. Johnson, V.M. Oversby, F. King, K. Spahiu, B. Grambow, D.W. Shoesmith, Swedish Nuclear Fuel and Waste Management Company Technical Record, TR-04-19, 2004.
[10] D.W. Shoesmith, J.J. Noël, F. Garisto, in: J.M. Hanchar, S. Stroes-Gascoyne, L. Browning (Eds.), Scientific Basis for Nuclear Waste Management XXVIII, Mater. Res. Soc. Symp. Proc., vol. 824, Warrendale, PA, 2004, pp. 81–87.

[11] S. Sunder, D.W. Shoesmith, N.H. Miller, J. Nucl. Mater. 244 (1997) 66–74.
[12] D.W. Shoesmith, S. Sunder, J.C. Tait, J. Nucl. Mater. 257 (1998) 89–98.
[13] F. King, M.J. Quinn, N.H. Miller, Swedish Nuclear Fuel and Waste Management Company Technical Report TR-99-27, 1999.
[14] S. Sunder, Atomic Energy of Canada Limited Report AECL-11380, COG-95-340, 1995.
[15] P. Carbol, J. Cobos-Sabate, J.-P. Glatz, C. Ronchi, V. Rondinella, D.H. Wegen, T. Wiss, A. Loida, V. Metz, B. Kienzler, K. Spahiu, B. Grambow, J. Quinones, A. Martinez, E. Valiente, Swedish Nuclear Fuel and Waste Management Technical Report TR-05-09, 2005.
[16] D.W. Shoesmith, Used fuel and uranium dioxide dissolution studies – a review, NWMO Report TR-2007-03, 2007.
[17] D.W. Shoesmith, M. Kolar, F. King, Corrosion 59 (2003) 802–816.
[18] D.W. Shoesmith, Canadian Nuclear Waste Management Organization Report TR-2008-19, 2008.
[19] P.C. Burns, R.C. Ewing, M.L. Miller, J. Nucl. Mater. 245 (1997) 1–9.
[20] E.C. Buck, R.J. Finch, P.A. Finn, J.K. Bates, in: I.G. McKinley, C. McCombie (Eds.), Scientific Basis for Nuclear Waste Management XXI, Mater. Res. Soc. Symp. Proc., vol. 506, Warrendale, PA, 1997, pp. 87–94.
[21] R.J. Finch, J.A. Fortner, E.C. Buck, S.F. Wolf, Neptunium incorporation into uranium(VI) compounds formed during aqueous corrosion of neptunium-bearing uranium oxides, in: B.P. McGrail, G.A. Cragnolino (Eds.), Scientific Basis for Nuclear Waste Management XXI, Mater. Res. Soc. Symp. Proc., vol. 713, Boston, MA, 2002, pp. 647–653.
[22] P.C. Burns, K.M. Deely, S. Skanthakumar, Radiochim. Acta 92 (2004) 151–159.
[23] W.-J. Cheong, P.G. Keech, Z. Qin, J.C. Wren, D.W. Shoesmith, Development of acidity in corroding nuclear fuel under waste disposal conditions, in: Darrell Dunn, Christophe Poinssot, Bruce Begg (Eds.), Scientific Basis for Nuclear Waste Management XXX, Mater. Res. Soc. Symp. Proc., vol. 985, Warrendale, PA, 2007, pp. 27–32.
[24] E.C. Buck, D.J. Wronkiewicz, P.A. Finn, J.K. Bates, J. Nucl. Mater. 249 (1997) 70–76.
[25] D.J. Wronkiewicz, J.K. Bates, T.J. Gerding, E. Veleckis, B.S. Tani, J. Nucl. Mater. 190 (1992) 107–127.
[26] D.J. Wronkiewicz, J.K. Bates, S.F. Wolf, E.C. Buck, J. Nucl. Mater. 238 (1996) 78–95.
[27] R.J. Finch, E.C. Buck, P.A. Finn, J.K. Bates, Oxidative corrosion of spent UO_2 fuel in vapor and dripping groundwater at 90 °C, in: D.J. Wronkiewicz, J.H. Lee (Eds.), Scientific Basis for Nuclear Waste Management XXII, Mater. Res. Soc. Symp. Proc., vol. 556, Warrendale, PA, 1999, pp. 431–438.
[28] Office of Civilian Radioactive Waste Management, ANL-EBS-MD-000015 Rev.02, 2004.
[29] R.J. Finch, R.C. Ewing, J. Nucl. Mater. 190 (1992) 133–156.
[30] R.J. Finch, R.C. Ewing, Radiochim. Acta 52/53 (1991) 395–401.
[31] C.N. Wilson, W.J. Gray, Effects of water composition on the dissolution rate of UO_2 under oxidizing conditions, in: V.M. Oversby, P.W. Brown (Eds.), Scientific Basis for Nuclear Waste Management, Mater. Res. Soc. Symp. Proc., vol. 176, Warrendale, PA, 1990, pp. 1431–1436.
[32] J.C. Tait, J.M. Luht, Ontario Hydro Report No. 06819-REP-01200-0006-R00, 1997.
[33] B.G. Santos, J.J. Noël, D.W. Shoesmith, Corros. Sci. 48 (2006) 3852–3868.
[34] B.G. Santos, J.J. Noël, D.W. Shoesmith, J. Nucl. Mater. 350 (2006) 320–331.
[35] P.C. Lucuta, R.A. Verrall, Hj. Matzke, B.J. Palmer, J. Nucl. Mater. 178 (1991) 48–60.
[36] B.G. Santos, H.W. Nesbitt, J.J. Noël, D.W. Shoesmith, Electrochim. Acta 49 (2004) 1863–1873.
[37] B.G. Santos, J.J. Noël, D.W. Shoesmith, Electrochim. Acta 51 (2006) 4157–4166.
[38] B.G. Santos, Ph.D. Thesis, The University of Western Ontario, London, Canada, 2005.
[39] J.A. Mandarino, Fleischer's Glossary of Mineral Species, eighth ed., Mineralogical Record Inc., Tucson, Arizona, 1999.
[40] H.R. Hoekstra, S. Siegel, J. Inorg. Nucl. Chem. 35 (1973) 761–779.
[41] L. Maya, G.M. Begun, J. Inorg. Nucl. Chem. 43 (1981) 2827–2832.
[42] F.V. Stohl, D.K. Smith, Am. Mineral. 66 (1981) 610–625.
[43] P.R. Graves, Appl. Spectrosc. 44 (1990) 1665–1667.
[44] G. Dolling, R.A. Cowley, A.D.B. Woods, Can. J. Phys. 43 (1965) 1397–1413.
[45] S.D. Senanayake, R. Rousseau, D. Colegrave, H. Idriss, J. Nucl. Mater. 342 (2005) 179–187.
[46] B.W. Biwer, W.L. Ebert, J.K. Bates, J. Nucl. Mater. 175 (1990) 188–193.
[47] J.I. Bullock, J. Chem. Soc. A (1969) 781–784.
[48] R.L. Frost, J. Cejka, M.L. Weier, W. Martens, J. Raman Spectrosc. 37 (2006) 538–551.
[49] A. Anderson, C. Chieh, D.E. Irish, J.P.K. Tong, Can. J. Chem. 58 (1980) 1651–1658.
[50] J. Čejka, Infrared spectroscopy and thermal analysis of the uranyl minerals, in: S.A.T. Redfern, M.A. Carpenter (Eds.), Transformation Processes in Minerals Reviews in Mineralogy and Geochemistry, vol. 38, Mineralogical Society of America, Washington, DC, 1999, pp. 521–622.
[51] S.V. Gevork'yan, A.O. Matkovskii, A.S. Povarennykh, G.A. Sidorenko, Mineral. Zh. 1 (1979) 78–81.
[52] P. McMillan, Am. Mineral. 69 (1984) 622–644.
[53] R.L. Frost, J. Čejka, M.L. Weier, W. Martens, J.T. Kloprogge, Spectrochim. Acta A 64 (2006) 308–315.
[54] S. Sunder, D.W. Shoesmith, R.J. Lemire, M.G. Bailey, G.J. Wallace, Corros. Sci. 32 (1991) 373–386.
[55] S. Sunder, N.H. Miller, D.W. Shoesmith, Corros. Sci. 46 (2004) 1095–1111.
[56] J.C. Wren, D.W. Shoesmith, S. Sunder, J. Electrochem. Soc. 152 (2005) B470–B481.
[57] D.W. Shoesmith, W.H. Hocking, S. Sunder, J.S. Betteridge, N.H. Miller, J. Alloys Compd. 213/214 (1994) 551–553.
[58] J.S. Goldik, J.J. Noël, H.W. Nesbitt, D.W. Shoesmith, Electrochim. Acta 49 (2004) 1699–1709.